Determining the Twist Angle of Stacked MoS_2 Layers using Machine Learning Assisted Low-Frequency Interlayer Raman Fingerprints

Jing Tang[1], Zifan Wang[2], Qishuo Tan[2], Jun Cao[2], Xi Ling[1,2,3,*]
[1]Division of Materials Science and Engineering, Boston University, Boston, Massachusetts 02215, USA
[2]Department of Chemistry, Boston University, Boston, Massachusetts 02215, USA
[3]The Photonics Center, Boston University, Boston, Massachusetts 02215, USA
Abstract
[*]Author to whom correspondence should be addressed: xiling@bu.edu

The investigation of twisted, stacked few-layer MoS_2 has revealed novel electronic, optical, and vibrational properties over an extended period. For the successful integration of twisted stacked few-layer MoS_2 into a wide range of applications, it is crucial to employ a non-invasive, versatile technique for characterizing the layered architecture of these complex structures. In this work, we introduce a machine learning-assisted low-frequency Raman spectroscopy method to characterize the twist angle of few-layer stacked MoS_2 samples. A feedforward neural network (FNN) is utilized to analyze the low-frequency breathing mode as a function of the twist angle. Moreover, using Finite difference method (FDM) and density functional theory (DFT) calculations, we show that the low frequency Raman spectra of MoS_2 are mainly influenced by the effect of the nearest and second nearest layers. A new improved linear chain model (TA-LCM) with taking the twist angle into the consideration is developed to understand the interlayer breathing modes of stacked few-layer MoS_2. This approach can be extended to other 2D materials systems and provides an intelligent way to investigate naturally stacked and twisted interlayer interactions.

KEYWORDS
Twisted Few-layer MoS_2, Low Frequency Raman Spectroscopy, FDM, DFT, Linear Chain Model

1|INTRODUCTION

Over the past decade, graphene and transition metal dichalcogenides (TMDs) have attracted significant attention due to their unique properties caused by the reduced dimension. Many more 2D materials are continuing emerging with a rainbow of intriguing physical properties including excellent photoluminescence (PL) emission[1] (e.g., MoS_2 and $MoSe_2$), superconductivity[2,3] (e.g., NbS_2 and TaS_2), magnetism[4–6] (e.g. CrI_3 and $NiPS_3$) and ferroelectricity[7,8] (e.g. $CuIn_2PS_6$). Moreover, stacking these 2D materials in different configurations - vertically or horizontally - leads to the formation of various homostructures and heterostructures with tunable electronic, optical, and magnetic properties[9–13].

Among the 2D materials, MoS_2 is one of the most widely studied semiconductors which shows promising potential in electronic and optoelectronic devices[14,15]. Generally, the number of layers, the stacking order, and stacking twist angle in 2D layers are critical factors in affecting the band structure[16] and the behavior of quasiparticles such as excitons[17–19] and some novel meso physical properties such as magnetism[20–23]. For instance, the stacking order significantly affects the second-harmonic signal (SHG) in stacked MoS_2 due to the net dipole moment induced by symmetry breaking[24]; For bilayer graphene with small twist angles, ultraheavy and ultrarelativistic quasiparticles were predicted from the theoretical works[25], and valleytronics induced by a moiré superlattice existing in twisted WSe_2 helps to develop and tune electric devices[26]. Recently, interfacial ferroelectricity by twisting 2D MoS_2 and nanomagnetism by twisting 2D magnetic materials were also reported[20,27]. Therefore, determining the twist angle in these 2D homostructures and heterostructures is vital for both fundamental study and the relevant applications.

Raman spectroscopy has emerged as an effective, versatile and convenient tool to probe the number of layers and twist angles in 2D materials and their heterostructures[28–30]. Particularly, the low-frequency Raman modes from the interlayer vibrations (usually below 100 cm^{-1}) in the 2D layers are very sensitive to the stacking configurations[31]. The number of modes is directly related to the number of layers, and the frequencies of the modes reflect the interlayer coupling strength which is strongly dependent on the stacking configurations[31]. Generally, twist angle affects the Raman shift by modifying the coupling strength between layers. Stronger coupling leads to a higher frequency of the modes and thus larger Raman shift. There are two types of interlayer vibrational modes. One is the breathing mode (BM) due to relative motion of the layers themselves parallel to their normal and the other is the shear mode (SM) due to the relative motion in a perpendicular direction to the normal[31]. The relationship between the twist angle and the low-frequency Raman modes has been investigated intensively [20,32–35]. For example, Rhea et al. reported that the low-frequency Raman is sensitive to few layered MoS_2 stacking configuration between layers[34]. These studies clearly show the power of low-frequency Raman spectra in determining the twist angle in 2D layers. However, relying on the published spectra on limited twist angles will not be able to provide information with desired accuracy. Moreover, there is still no physical equation to elaborate the relationship between Raman shift and twist angle. A continuum model[36] having been developed to assign the SM and BM position from 0° to 20° is limited. To

address this challenge, we utilized a machine learning approach to map low-frequency Raman spectra features to the twist angle and developed an improved linear chain model[35,37–40] that considers the effects of twist angle and near layers. We use a feedforward neural network (FNN)[41] to obtain a function to describe the relationship between the low-frequency modes and the twist angle, and then use finite difference method (FDM)[42] and density functional theory (DFT) calculation to show that the nearest and second-nearest layer plays the most crucial role in low-frequency modes. The resulting model can be used to accurately characterize the twist angle in stacked few-layer MoS_2 and other 2D systems, providing valuable insights into interlayer coupling.

2|MATERIALS AND METHODS

2.1|Fabrication of Twisted Bilayer MoS_2

Seeding promoter assisted chemical vapor deposition (CVD) was utilized to synthesize MoS_2 monolayers[43]. In our synthesis, two crucibles containing the molybdenum trioxide (MoO_3) and sulfur (S) powders as precursors, were separated in a single quartz tube. A 300 nm SiO_2/Si substrate was positioned face-down on the crucible loaded with MoO_3, where the seeding promoter, perylene-3,4,9,10-tetracarboxylic acid tetrapotassium salt (PTAS), was applied on the SiO_2/Si substrate surface. The temperature was increased from room temperature to 620℃ in 30 minutes and maintained at 620℃ for 5 minutes in 17 sccm Ar carrier gas flow. The sample was then cooled down immediately to room temperature in 100 sccm Ar carry gas flow.

We further used dry transfer to stack two MoS_2 monolayers together to form the twist bilayers[44]. In brief, a monolayer of MoS_2 synthesized via CVD on a SiO_2/Si substrate is spin-coated with a 20% Polystyrene (PS) toluene solution, followed by baking at 80 ℃ for 3 minutes. The sample is then placed in water for 10 minutes, causing the PS film together with the MoS_2 monolayer to separate from the substrate and float on the water surface. Subsequently, a polydimethyl-siloxane (PDMS) elastomer is used to pick up the film, forming a PDMS-PS-MoS_2 (PPM) structure. The top glass slide of the transfer platform is then connected to the PPM and carefully placed on top of another monolayer of MoS_2 on a Si/SiO_2 substrate. After baking at 90℃ for 10 minutes, the top glass slide is carefully lifted, leaving the monolayer MoS_2 on the bottom substrate. Because there are multiple monolayers of MoS_2 triangular domains on one substrate with different crystal orientation, the resulting stacked MoS_2 bilayers have various twist angles for the study.

To determine the twist angle, we leverage the fact that the side of the triangular domain aligns with the lattice direction. Thus, by gauging the rotating angle between two triangular domains under the optical microscopy image, we can measure the twist angle in the bilayer MoS_2.This method provides a precision within 3^{o}.

2.2|Raman spectroscopic characterization

Raman spectroscopy measurements were conducted using a Horiba T64000 triple mode spectrometer equipped with an 1800 g/mm grating and a liquid nitrogen-cooled CCD camera for signal detection. A 532 nm laser was used to excite the samples, and Raman spectra were measured in the range of 12 cm^{-1} to 550 cm^{-1}, which included both low-frequency (LF) and high-frequency (HF) featured Raman peaks of MoS_2. 532nm laser with 2.33 eV energy is used here because it is the most commonly available laser in most research laboratories, which makes our results be more applicable and representative. Additionally, a Raman peak from the Si substrate at 520.7 cm^{-1} was

also included for the calibration of the spectra.

2.3|Machine Learning Methods

We employed a FNN[45] (Fig.2a) with a structure of 187 input nodes, two hidden layers with 64 and 32 nodes respectively, and one output node. The blue dots represent neurons. The solid lines connecting the dots represent the flow of information between the neurons. The weights and biases (not shown here) associated with these connections determine the strength and offset of the computations performed by the neurons. By adjusting these weights and biases during training, the network learns to predict twist angle based on the input Raman spectra. The FNN was trained using a backpropagation algorithm with a mean squared error (MSE) loss function to model the relationship between the input low-frequency spectrum and the material property (i.e. twist angle). In this study, the input nodes are the low frequency Raman spectra and the output is twist angle (θ_t). The hidden layers allow the FNN to capture complex nonlinear relationships between the input parameters and the output property. 50 different Raman low-frequency spectra are collected as training dataset and 5 more spectra are for test. We optimize the hyperparameters of the FNN by Adam[46], including the number of nodes in each layer and the learning rate, through a cross-validation procedure to realize the best performance (See Supporting Materials Section 2). The trained FNN was then used to predict θ_t from the low frequency Raman spectra with high accuracy (margin of error = 4.7%) and efficiency.

2.4|DFT Calculation Methods

To investigate the vibrational mechanism related to low frequency Raman modes in few-layer MoS_2 systems, first-principles calculations based on density functional theory (DFT) were conducted. The Quantum Espresso package was employed to perform the DFT calculations with the Perdew-Burke-Ernzerhof (PBE) functional serving as the exchange-correlation functional. In order to simulate a 2D system, a 15 Å vacuum layer was utilized. A uniform 9×9×1 K-point grid was employed for integration over the Brillouin zone. Systems consisting of 4 layers of 2H-MoS_2 were investigated. To understand the effect of each layer in a multilayer system on the targeting layer, finite displacement method (FDM)[42] is used to calculate the spring constant (Fig.3a). The interlayer spring constant can be obtained by calculating the force acting on the targeting layer of MoS_2 when the other layer is displaced by a small distance in the direction perpendicular to the layer plane. The interlayer spring constant can then be calculated as the ratio of the force to the displacement, which is $k = \frac{F}{\Delta x}$, where k is the spring constant, F is the force, and Δx is the finite small displacement In this work, we show 5 different small finite displacements of the top layer and calculate the out-of-plane force operating on each other layer to study the effect of the force in each layer on the top layer.

3|RESULTS AND DISCUSSION

3.1|Experimental Raman characteristic of twisted bilayer MoS_2 as training dataset

Figure 1a shows a typical optical image of the twisted bilayer MoS_2, where the highlighted two triangular domains are stacked and the twist angle is determined to be 9°. Figure 1b illustrate the vibrations for SM and BM in the bilayer. These interlayer

vibrational modes have been reported at the low-frequency region of the Raman spectra (<100 cm^{-1})[32]. In the Raman spectrum of monolayer MoS_2, low-frequency peaks are absent due to the lack of interlayer coupling within the monolayer system. In contrast, bilayer MoS_2 exhibits both SM (20 cm^{-1}) and BM (38 cm^{-1}) (Fig.1c). The characteristic high-frequency peaks of MoS_2, the E_{2g} mode (at 385 cm^{-1} for monolayer MoS_2) and the A_{1g} mode (at 404 cm^{-1} for monolayer MoS_2) are observed in both exfoliated monolayer and bilayers (Fig.1c). Fig.1d and 1e show the low-frequency and high-frequency Raman spectra of bilayer MoS_2 with various twist angle. It is clear that the high-frequency modes are not sensitive to the twist angle, however, the low frequency modes are strongly dependent on the twisted angle, which is consistent with the phenomenon reported in literature[32]. For example, at θ=60° both the SM and BM can be seemed clearly, at θ=9°, 20°, 29° and 41°, only the BMs are visible. Such high sensitivity of the interlayer vibrational mode to the twist angle is due to the varying symmetries at different angles.[32] The monolayer MoS_2 belongs to the D_{6h} point group. Upon twisting the layers, the symmetry will be reduced to different extend, resulting in the change of the low-frequency Raman modes.

At specific twist angles, known as commensurate angles[47], the lattice of the bilayer MoS_2 system exhibits an overall periodicity, leading to a long-range Moiré pattern (See Supporting Materials Section 1). This pattern can be characterized by a larger supercell with its own unique symmetry. In such cases, the low-frequency Raman modes are easier to be observed due to the considerable vibrational modes whose supercell's symmetry satisfying the Raman selection rules. At the twist angles near 0° and 60°, a higher prevalence of commensurate angles is observed. As depicted in Fig.1d when the twist angle approaches 0° and 60°, the SM and BM manifest distinctly. In contrast, at incommensurate angles, where the Moiré pattern lacks long-range order, the twisted bilayers result in a breakdown of the original lattice symmetry[33,48], and the Raman selection rules become more complicated, leading to the emergence of shift or disappearance of low-frequency modes. As shown in Fig.1d, when the twist angle is approaching 30°, the SM and BM tend to merge, resulting in a single broad peak. Moreover, these modes might become too weak to be observed due to the mismatch of the lattices leading to weak interlayer coupling[32]. For example, at 20°, the low-frequency Raman peaks become weaker than that of other twist angles. Considering the distinct low-frequency Raman spectra at different twist angles, it is impossible to measure the Raman spectra for all twisted 2D systems experimentally. Thus, it is often lack of reference when trying to identify the twist angle from the measured Raman spectra. In this work, we use the measured 50 low-frequency Raman spectra to train the FNN to build the relationship with the twist angle.

3.2| FNN to predict twist angle from low frequency spectrum

To determine the relationship R=f(θ_t) between the low-frequency Raman spectrum (R) and the twist angle (θ_t) from 0° to 60° in bilayer MoS_2, we employed a designed FNN model, referred as the twist angle dependent FNN (TA-FNN). Figure 2a illustrates the TA-FNN architecture, consisting of one input layer, two hidden layers, and one output layer. The well-trained neural network is capable of predicting the twist angle in bilayer MoS_2 based on the low-frequency Raman spectra. Figure 2b compares the predicted θ_t

from the model with the real θ_t. The solid line along the diagonal is a reference line where the predictions exactly match with the real value. Due to the inevitable measurement errors, interlayer impurities, and model robustness, the predictions are deviates from the reference line. However, all predictions in the test dataset exhibit a credible 5% error margin, suggesting that the model can predict the twist angle with high integrity. Therefore, the TA-FNN demonstrates the close relationship between the Raman spectrum and the twist angle effectively.

To establish R as a function of θ_t (R=f (θ_t)), we first obtain a regression mapping of θ to the breathing mode spring constant, which comes from the BM peak position. In Figure 2c, a function

$$R=-2.6*10^{-8}*\theta_t^6+4.6*10^{-6}*\theta_t^5-3.1*10^{-4}*\theta_t^4+8.9*10^{-3}*\theta_t^3-1.1*10^{-1}*\theta_t^2+3.1*\theta_t+3.7$$

is shown as a sixth order polynomial fitting line to visualize the twist angle-dependent spring constant trend. To obtain a better fit, the data used in the fitting process are often pre-processed to remove some fluctuations. One common approach[49] is to calculate the average value of the data within a specified range, which is then assigned as the representative data point for that range in the fitting. For instance, in this fitting process, the average value of the LF peak positions between 10° to 20° is assigned as the representative value for 15° LF mode position in the fitting. The spring constant is then calculated from the BM frequency using the linear chain model (see Supporting Materials Section 3). It is noteworthy that the fitting line exhibits a periodicity of 30°, which is attributed to the fact that twisted stacking lattices are the same for θ_t=0° and 60° (both form 3R and 2H stacking), and they transform into 1T or 3R when the twist angle is 30° if not considering translational shift[32]. In the final model, this fitting formula is incorporated to account for the influence of the twist angle.

3.3|Investiagtion of the contribution of near layers to the interlayer coupling

To implement the model in multilayered materials, the coupling strength between layers should be studied. Theoretically, every two layers have coupling between them. However, since each layer is at a different distance away from the interested layer, the intermediate layers screen the Coulomb force, causing the nearest layer from the target layer to predominantly contribute to the spring constant of target layer. We perform density functional theory (DFT) calculations and finite difference method (FDM) to compute the reduced spring constant.

Figure 3a shows a four-layer 2H-MoS_2 system. From linear chain mode, the system can be simplified by considering interlayer coupling as a spring constant. The nearest interlayer spring constant is assigned to γ_1, the second nearest interlayer spring constant is γ_2 and the third nearest is γ_3. Using FDM, we introduce a small vertical displacement Δx to the top layer and calculate the forces operated on the 2nd, 3rd and 4th layer by DFT, which reflect operation strength from each layer.

Displacing the top layer with varying distances of 0.027 Å, 0.054 Å, 0.081 Å, 0.108 Å, and 0.135 Å is performed. The amplitudes of the atomic displacements are limited to 1%[50,51]. Figure 3b illustrates the force per unit area resulting from different top layer displacements, denoted by different colored dashed lines. First, larger layer displacement corresponds to increased forces due to the augmented strain within the

system. Take nearest layer spring constant for example, when the smallest displacement 0.027Å is applied on the top layer, the force on the nearest layer is 3.5×10^{-4}eV/Å. Comparably, the largest displacement 0.135Å generate 2.4×10^{-3} eV/Å force on the nearest layer, which is 6.8 times that of previous one. From Hook's law, force should be proportional to displacement linearly, hence, it is reasonable when displacement increase to 5 times large, the force increases to 6.8 times because the vibration of layer is nonharmonic. Second, we find that the nearest layer contributes to force on the interested layer by nearly an order of magnitude compared to the second nearest layer, and two orders of magnitude compared to the third nearest layer for the four larger displacements. For the smallest displacement of 0.027 Å, the force exerted by the nearest layer is 3.5×10^{-4} eV/Å, while the second nearest layer exerts a force of 1.9×10^{-4} eV/Å, approximately half of that by the nearest layer. The force exerted by the third nearest layer is 1.0×10^{-6} eV/Å, which is much smaller - about 1/350 of the force generated by the nearest layer. For larger displacement like 0.081Å, the nearest layer force is 1.6×10^{-3}eV/Å, and the 2nd layer force is 1.0×10^{-4} eV/Å, which is 1/16 of nearest layer. The 3rd layer force is 7×10^{-5} eV/Å, which is 4% of the nearest layer. Therefore, it's reasonable to simplify the linear chain model by just considering the nearest layer and second nearest layer effect. From the force *vs* layers relationship, the forces are fluctuating and close to zero for the 3rd nearest layer. This is because the strong Coulomb screening of the near layers weaken the coupling for the layers far from it. Therefore, we only considered the nearest and second nearest layer coupling in the final model.

3.4|Twist Angle Dependent Linear Chain Model for Interlayer Modes

Based on the above analysis, the vibrational modes can be based on the coupling between layers whose strength is closely related to twist angles. Therefore, a twist angle dependent linear chain model (TA-LCM) was established in this section to give more precise low-frequency BM positions. Because SM cannot be observed from 10° to 48° in twist bilayer MoS_2 in our experiment, it will be discussed qualitatively in later context. TA-LCM is based on classical LCM and introduce twist angle dependent spring constant in the dynamic matrix (See Supporting Materials Section 4). TA-LCM is visualized in Fig.4a in a 1+1+1 twisted trilayer model system. Nearest layer coupling depends on twisted angle effect is shown by the clouds between two layers. In the model, consider $\gamma(\theta_t)$ as the spring constant. The dynamic matrix will be

$$\begin{bmatrix} \gamma_1(\theta_1)+\gamma_2(\theta_3) & -\gamma_1(\theta_1) & -\gamma_2(\theta_3) \\ -\gamma_1(\theta_1) & \gamma_1(\theta_1)+\gamma_1(\theta_2) & -\gamma_1(\theta_2) \\ -\gamma_2(\theta_3) & -\gamma_1(\theta_2) & \gamma_1(\theta_2)+\gamma_2(\theta_3) \end{bmatrix}$$

This model can be applied on all twisted stacking system well by changing the matrix element in the dynamic matrix and calculating the eigenvalues as the vibration frequencies. Figure 4b shows the optical image of a 1+1+1 twisted trilayer MoS_2. A second dry transfer is implemented here to stack the third MoS_2 triangle sample vertically on an existing twist bilayer MoS_2. The twist angles θ_1, θ_2 are measured as 42° and 28° for the twist trilayer MoS_2 sample in Fig. 4b. Replacing θ_1, θ_2 and θ_3 with 42°, 28° and 50° (calculated by 120°-(42°+28°)) in previous dynamic matrix, the calculated BM with lower frequency (BM1) and breathing mode with higher frequency

(BM2) are 34.5 cm^{-1} and 47.0 cm^{-1}. Figure 4c shows the experimental low-frequency spectrum for the sample in Fig. 4b. Peak BM1 (34.3 cm^{-1}) and peak BM2 (47.1 cm^{-1}) match the predicted BMs well. For more twisted trilayer samples, please see Supporting Materials Section 5. Other than BMs, the peak with lowest frequency at 23.9 cm^{-1} is assigned to a SM because previous work proved that SM is usually not affected by the twist angle. Here the system containing a 50° twist angle will generate a SM around 28.3 cm^{-1}. Twist angle 28° is not a commensurate angle, so it cannot couple to above twisted bilayer shearing system. Another evidence is when a lower excitation power (500 μW) is used, the SM disappears and when a higher power (1 mW) is applied, it appears clearly. Such power dependence is because the entire MoS_2 layer needs to participate to excite SM, thus needs more power. In contrast, exciting BM can be a local event. This also results in the larger reduced mass of SM than that of BM. From the most straightforward vibration theory $f = \sqrt{\frac{\gamma}{m}}$, where f is the vibration frequencies, γ is the spring constant and m is the mass, larger mass leads to lower vibrational frequency. Therefore, the SM usually exhibits lower Raman shift than the BM, matching well with our assignment.

Furthermore, Fig. 4d shows a contour map of the prediction results of the frequency of the BMs for twist trilayer MoS_2 from our model. θ_1 and θ_2 are the two twist angles in the trilayer ranging from 0° to 60°, from where we predict the BM1 and BM2 frequencies. It is reasonable to see BM1 and BM2 has the similar Raman shift trend according to twist angles. When θ_1 and θ_2 are both around 30°, the Raman shift of BM1 and BM2 are the largest in the whole (θ_1,θ_2) region. When both twist angles are close to 0° and 60°, the BM1 and BM2 Raman shifts are local maxima compared to their nearby angles. This is because the coupling around these special angles is stronger. As commensurate angles appears more around 0° and 60°[47], lattice periodicity in superlattice creates stronger coupling between layers and generates higher vibrational frequency. Although we demonstrate the application of this model in a twist trilayer MoS_2 to predict the mode frequencies from the twist angles, it can be applied to predict the twist angle from low-frequency Raman modes or obtain low-frequency Raman information (e.g. mode frequency) from the stacking configuration in other trilayer 2D materials systems.

4|CONCLUSION

In conclusion, we have successfully applied a machine learning approach to elucidate the relationship between the spring constant and the twist angle, which then is further used to predict the twist angle in stacked 2D layers from the measured low-frequency Raman spectra. Moreover, we performed FDM and DFT calculations to show that only the nearest layer plays significant role in the linear chain model. Furthermore, we applied the TA-LCM on a twist (1+1+1) trilayer MoS_2 sample to validate the improved identification of low-frequency Raman BMs from the given twist angles. This methodology can be extended to investigate other 2D materials with twisted stacking, thereby enhancing our understanding of low-frequency vibration modes and facilitating the characterization of these materials' structure and properties.

CONFLICTS OF INTEREST

There are no conflicts to declare.

ACKNOWLEDGMENTS

Research is primarily supported by the U.S. Department of Energy (DOE), Office of Science, Basic Energy Sciences (BES), under Award DE-SC0021064. X.L. acknowledges the membership of the Photonics Center at Boston University. Work by Q.S.T and X.L. is supported by the National Science Foundation (NSF) under Grant No. (1945364).

ORCID

Xi Ling: 0000-0003-3462-9088

REFERENCES

[1] H. Nan, Z. Wang, W. Wang, Z. Liang, Y. Lu, Q. Chen, D. He, P. Tan, F. Miao, X. Wang, J. Wang, Z. Ni, *ACS Nano* **2014**, *8*, 5738.

[2] E. Navarro-Moratalla, J. O. Island, S. Mañas-Valero, E. Pinilla-Cienfuegos, A. Castellanos-Gomez, J. Quereda, G. Rubio-Bollinger, L. Chirolli, J. A. Silva-Guillén, N. Agraït, G. A. Steele, F. Guinea, H. S. J. van der Zant, E. Coronado, *Nat Commun* **2016**, *7*, 11043.

[3] R. Yan, G. Khalsa, B. T. Schaefer, A. Jarjour, S. Rouvimov, K. C. Nowack, H. G. Xing, D. Jena, *Appl. Phys. Express* **2019**, *12*, 023008.

[4] X. Wang, J. Cao, H. Li, Z. Lu, A. Cohen, A. Haldar, H. Kitadai, Q. Tan, K. S. Burch, D. Smirnov, W. Xu, S. Sharifzadeh, L. Liang, X. Ling, *Science Advances* **2022**, *8*, eabl7707.

[5] X. Wang, J. Cao, Z. Lu, A. Cohen, H. Kitadai, T. Li, Q. Tan, M. Wilson, C. H. Lui, D. Smirnov, S. Sharifzadeh, X. Ling, *Nat. Mater.* **2021**, *20*, 964.

[6] Y. Xu, A. Ray, Y.-T. Shao, S. Jiang, K. Lee, D. Weber, J. E. Goldberger, K. Watanabe, T. Taniguchi, D. A. Muller, K. F. Mak, J. Shan, *Nat. Nanotechnol.* **2022**, *17*, 143.

[7] J. Wu, H.-Y. Chen, N. Yang, J. Cao, X. Yan, F. Liu, Q. Sun, X. Ling, J. Guo, H. Wang, *Nat Electron* **2020**, *3*, 466.

[8] Q. Wang, T. Xie, N. A. Blumenschein, Z. Song, J. C. Kotsakidis, A. T. Hanbicki, M. A. Susner, B. S. Conner, Q. Tan, S. H. Lee, Z. Mao, X. Ling, T. Low, J.-P. Wang, A. L. Friedman, C. Gong, *Matter* **2022**, *5*, 4425.

[9] D. Li, J. Tan, H. Qu, Y. Li, Y. Gong, S. Zhang, H. Mao, Q. Bao, Y. Zhang, G. P. Wang, *Matter* **2022**, *5*, 3452.

[10] K. Yao, N. R. Finney, J. Zhang, S. L. Moore, L. Xian, N. Tancogne-Dejean, F. Liu, J. Ardelean, X. Xu, D. Halbertal, K. Watanabe, T. Taniguchi, H. Ochoa, A. Asenjo-Garcia, X. Zhu, D. N. Basov, A. Rubio, C. R. Dean, J. Hone, P. J. Schuck, *Science Advances* **2021**, *7*, eabe8691.

[11] X. Li, H. Liu, C. Ke, W. Tang, M. Liu, F. Huang, Y. Wu, Z. Wu, J. Kang, *Laser & Photonics Reviews* **2021**, *15*, 2100322.

[12] J. Tan, S. Li, B. Liu, H.-M. Cheng, *Small Structures* **2021**, *2*, 2000093.

[13] T. Vincent, J. Liang, S. Singh, E. G. Castanon, X. Zhang, A. McCreary, D. Jariwala, O. Kazakova, Z. Y. A. Balushi, *Applied Physics Reviews* **2021**, *8*, 041320.

[14] M. Timpel, G. Ligorio, A. Ghiami, L. Gavioli, E. Cavaliere, A. Chiappini, F. Rossi, L. Pasquali, F. Gärisch, E. J. W. List-Kratochvil, P. Nozar, A. Quaranta, R. Verucchi, M. V. Nardi, *npj 2D Mater*

Appl **2021**, *5*, 1.
[15] J. Pak, I. Lee, K. Cho, J.-K. Kim, H. Jeong, W.-T. Hwang, G. H. Ahn, K. Kang, W. J. Yu, A. Javey, S. Chung, T. Lee, *ACS Nano* **2019**, *13*, 9638.
[16] C. Zhang, C.-P. Chuu, X. Ren, M.-Y. Li, L.-J. Li, C. Jin, M.-Y. Chou, C.-K. Shih, *Science Advances* **2017**, *3*, e1601459.
[17] H. Yu, Y. Wang, Q. Tong, X. Xu, W. Yao, *Phys. Rev. Lett.* **2015**, *115*, 187002.
[18] K. Tran, G. Moody, F. Wu, X. Lu, J. Choi, K. Kim, A. Rai, D. A. Sanchez, J. Quan, A. Singh, J. Embley, A. Zepeda, M. Campbell, T. Autry, T. Taniguchi, K. Watanabe, N. Lu, S. K. Banerjee, K. L. Silverman, S. Kim, E. Tutuc, L. Yang, A. H. MacDonald, X. Li, *Nature* **2019**, *567*, 71.
[19] C. Jin, E. C. Regan, A. Yan, M. Iqbal Bakti Utama, D. Wang, S. Zhao, Y. Qin, S. Yang, Z. Zheng, S. Shi, K. Watanabe, T. Taniguchi, S. Tongay, A. Zettl, F. Wang, *Nature* **2019**, *567*, 76.
[20] T. Song, Q.-C. Sun, E. Anderson, C. Wang, J. Qian, T. Taniguchi, K. Watanabe, M. A. McGuire, R. Stöhr, D. Xiao, T. Cao, J. Wrachtrup, X. Xu, *Science* **2021**, *374*, 1140.
[21] K. Hejazi, Z.-X. Luo, B. Leon, *PNAS* **2020**, *117*, 10721.
[22] Q. Tong, F. Liu, J. Xiao, W. Yao, *Nano Lett.* **2018**, *18*, 7194.
[23] C. Wang, Y. Gao, H. Lv, X. Xu, D. Xiao, *Phys. Rev. Lett.* **2020**, *125*, 247201.
[24] S. M. Shinde, K. P. Dhakal, X. Chen, W. S. Yun, J. Lee, H. Kim, J.-H. Ahn, *NPG Asia Mater* **2018**, *10*, e468.
[25] S. Carr, C. Li, Z. Zhu, E. Kaxiras, S. Sachdev, A. Kruchkov, *Nano Lett.* **2020**, *20*, 3030.
[26] G. Scuri, T. I. Andersen, Y. Zhou, D. S. Wild, J. Sung, R. J. Gelly, D. Bérubé, H. Heo, L. Shao, A. Y. Joe, A. M. Mier Valdivia, T. Taniguchi, K. Watanabe, M. Lončar, P. Kim, M. D. Lukin, H. Park, *Phys. Rev. Lett.* **2020**, *124*, 217403.
[27] X. Wang, K. Yasuda, Y. Zhang, S. Liu, K. Watanabe, T. Taniguchi, J. Hone, L. Fu, P. Jarillo-Herrero, *Nat. Nanotechnol.* **2022**, *17*, 367.
[28] M. Zhang, N. Han, J. Zhang, J. Wang, X. Chen, J. Zhao, X. Gan, *Science Advances* **2023**, *9*, eadf4571.
[29] L. M. Malard, L. Lafeta, R. S. Cunha, R. Nadas, A. Gadelha, L. Gustavo Cançado, A. Jorio, *Physical Chemistry Chemical Physics* **2021**, *23*, 23428.
[30] X. Cong, X.-L. Liu, M.-L. Lin, P.-H. Tan, *npj 2D Mater Appl* **2020**, *4*, 1.
[31] L. Liang, J. Zhang, B. G. Sumpter, Q.-H. Tan, P.-H. Tan, V. Meunier, *ACS Nano* **2017**, *11*, 11777.
[32] S. Huang, L. Liang, X. Ling, A. A. Puretzky, D. B. Geohegan, B. G. Sumpter, J. Kong, V. Meunier, M. S. Dresselhaus, *Nano Lett.* **2016**, *16*, 1435.
[33] A. A. Puretzky, L. Liang, X. Li, K. Xiao, B. G. Sumpter, V. Meunier, D. B. Geohegan, *ACS Nano* **2016**, *10*, 2736.
[34] R. T. Sam, T. Umakoshi, P. Verma, *Sci Rep* **2020**, *10*, 21227.
[35] X. Zhou, K. Jin, X. Cong, Q. Tan, J. Li, D. Liu, J. Luo, *Journal of Colloid and Interface Science* **2019**, *538*, 159.
[36] J. Quan, L. Linhart, M.-L. Lin, D. Lee, J. Zhu, C.-Y. Wang, W.-T. Hsu, J. Choi, J. Embley, C. Young, T. Taniguchi, K. Watanabe, C.-K. Shih, K. Lai, A. H. MacDonald, P.-H. Tan, F. Libisch, X. Li, *Nat. Mater.* **2021**, *20*, 1100.
[37] X. Zhang, W. P. Han, J. B. Wu, S. Milana, Y. Lu, Q. Q. Li, A. C. Ferrari, P. H. Tan, *Phys. Rev. B* **2013**, *87*, 115413.
[38] X. Zhang, X.-F. Qiao, W. Shi, J.-B. Wu, D.-S. Jiang, P.-H. Tan, *Chem. Soc. Rev.* **2015**, *44*, 2757.

[39] J.-B. Wu, X. Zhang, M. Ijäs, W.-P. Han, X.-F. Qiao, X.-L. Li, D.-S. Jiang, A. C. Ferrari, P.-H. Tan, *Nat Commun* **2014**, *5*, 5309.
[40] X. Zhang, W.-P. Han, X.-F. Qiao, Q.-H. Tan, Y.-F. Wang, J. Zhang, P.-H. Tan, *Carbon* **2016**, *99*, 118.
[41] D. Svozil, V. Kvasnicka, J. Pospichal, *Chemometrics and Intelligent Laboratory Systems* **1997**, *39*, 43.
[42] C. Grossmann, H.-G. Roos, M. Stynes, *Numerical Treatment of Partial Differential Equations*, Springer, Berlin, Heidelberg, **2007**.
[43] X. Ling, Y.-H. Lee, Y. Lin, W. Fang, L. Yu, M. S. Dresselhaus, J. Kong, *Nano Lett.* **2014**, *14*, 464.
[44] Z.-Q. Xu, Y. Zhang, S. Lin, C. Zheng, Y. L. Zhong, X. Xia, Z. Li, P. J. Sophia, M. S. Fuhrer, Y.-B. Cheng, Q. Bao, *ACS Nano* **2015**, *9*, 6178.
[45] V. K. Ojha, A. Abraham, V. Snášel, *Engineering Applications of Artificial Intelligence* **2017**, *60*, 97.
[46] D. P. Kingma, J. Ba, arXiv preprint, **2017**, arXiv:1412.6980.
[47] W. Yao, Er. Wang, C. Bao, Y. Zhang, K. Zhang, K. Bao, C. Chan, C. Chen, J. Avila, M. C. Asensio, J. Zhu and S. Zhou, PNAS **2018**, 116, 6928.
.[48]J. Holler, S. Meier, M. Kempf, P. Nagler, K. Watanabe, T. Taniguchi, T. Korn, C. Schüller, *Applied Physics Letters* **2020**, *117*, 013104.
[49] G.-F. Gu, W.-X. Zhou, *Phys. Rev. E* **2010**, *82*, 011136.
[50] G. Kresse, J. Furthmüller, J. Hafner, *EPL* **1995**, *32*, 729.
[51] K. Parlinski, Z. Q. Li, Y. Kawazoe, *Phys. Rev. Lett.* **1997**, *78*, 4063.

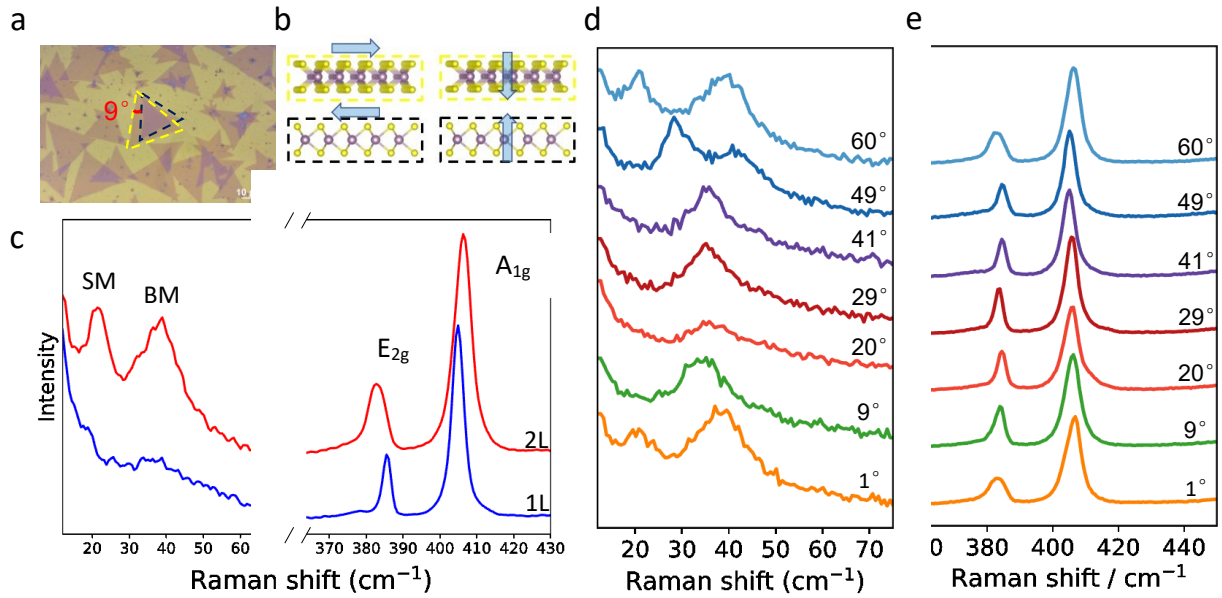

Fig.1 (a) Optical image of twisted bilayer MoS_2 on 300 nm SiO_2/Si substrate. (b) Illustration of the shear mode and the breathing mode in bilayer MoS_2. (c) Raman spectra of exfoliated monolayer MoS_2 and bilayer 2H-MoS_2. (d) Low-frequency Raman spectra in bilayer MoS_2 with different twist angles labeled on the spectra. (e) High-frequency Raman spectra showing the E_{2g} and A_{1g} modes.

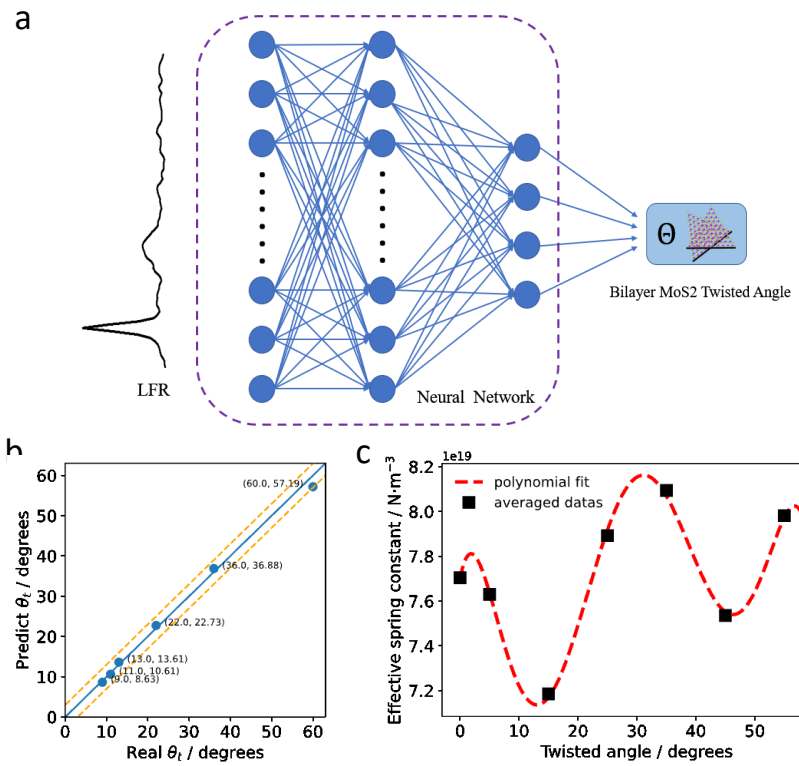

Fig.2 (a) The artificial neural network (FNN) architecture, in which the low-frequency Raman spectrum serves as the input and the twist angle as the output. (b) Plot of the relationship between the predictions and the real values. Blue dots represent the predictions generated by the TA-FNN. The blue solid line signifies the ideal match between the predictions and the real values. The dashed lines delineate the 5% error region. (c) The effective spring constant as a function of the twist angle. The polynomial fitting line is indicated.

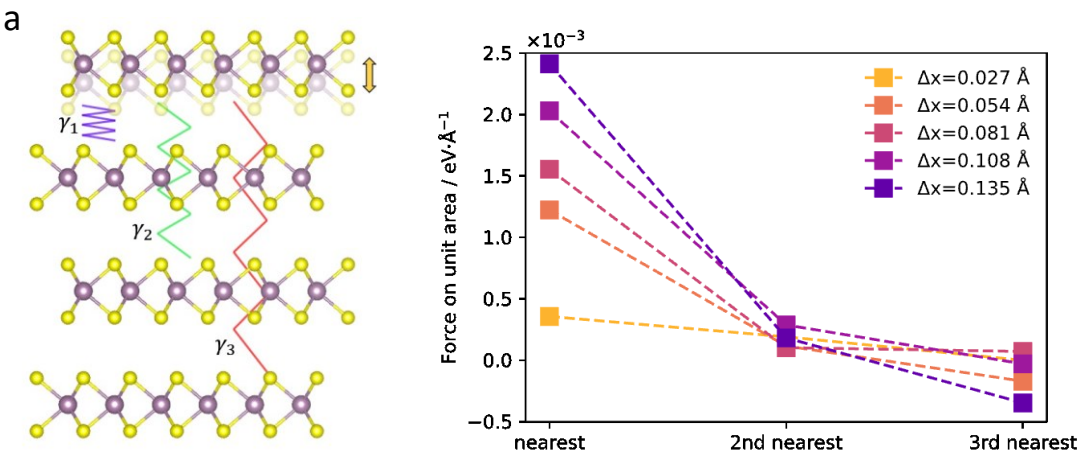

Fig.3 (a) Illustration of the interlayer coupling from the nearest, the second nearest and the third nearest layers. A finite small displacement Δx is applied to the top layer. Nearest, second nearest and third nearest spring constant γ_1, γ_2 and γ_3 are shown between the corresponding layers. (b) The force on unit area calculated by DFT and FDM for five Δx.

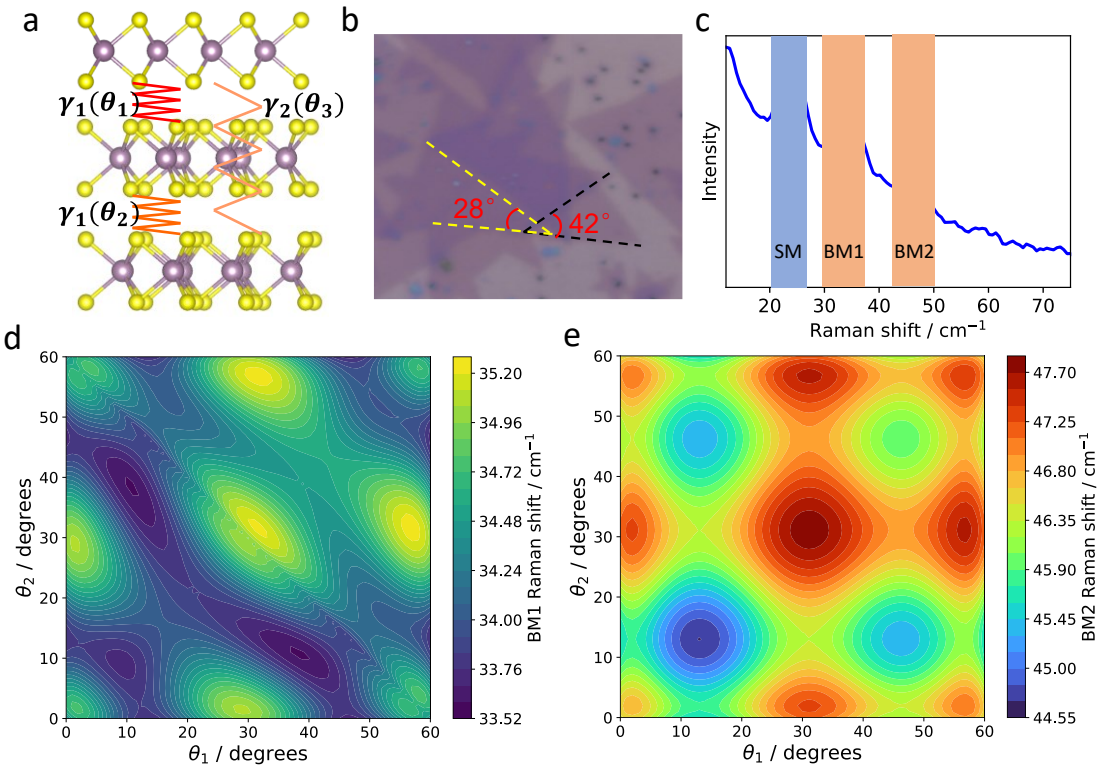

Fig.4 (a) 1+1+1 twisted trilayer MoS_2 TA-LCM schema. θ_1, θ_2 and θ_3 are twist angle between the 1st and 2nd layer, 2nd and 3rd layer, and 1st and 3rd layer. (b) Optical image of one 1+1+1 twisted trilayer MoS_2. (c) Low-frequency Raman spectrum of the 1+1+1 twisted trilayer MoS_2 shown in (b). (d, e) Contour maps of BM1 and BM2 peak position calculated from TA-LCM.